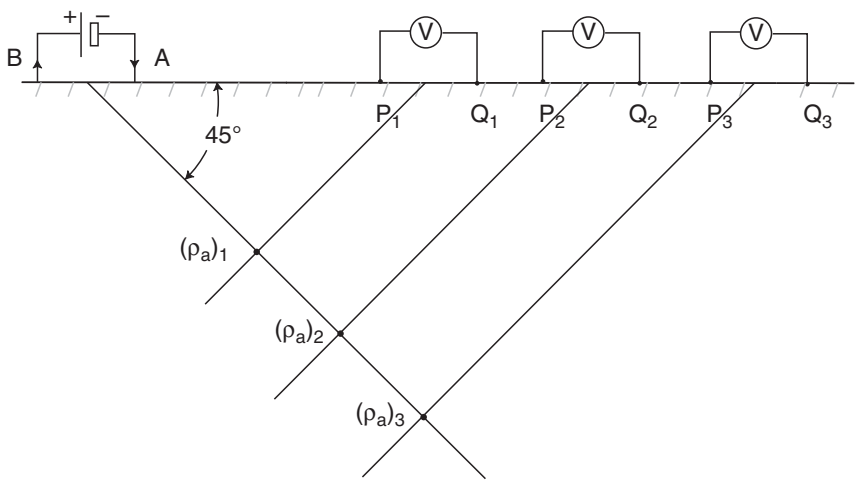

Figure 4.15 Construction of a dipole–dipole resistivity pseudosection.

4.6 Resistivity pseudosections

A convenient way to display multi-electrode resistivity data is by means of a resistivity pseudosection. As shown in Figure 4.15, the measured apparent resistivity ρ_a associated with a current AB and a potential electrode pair PQ is plotted at the intersection of two lines, each making a 45° angle with the ground surface and passing through the center of one of the electrode pairs. This procedure is repeated for each pair of current and potential electrodes. The resulting pseudosection provides a rough indication of the true Earth resistivity since the maximum sensitivity to the ground structure of a given voltage measurement occurs close to the midpoint of the four-electrode configuration at a depth of approximately one-half the separation of the current–potential electrode pairs.

To provide an example of resistivity imaging, a dataset was acquired using the multi-electrode Sting R8/IP system (www.agiusa.com), as illustrated in Figure 4.16. The acquisition protocol involved a computer-controlled sequence of Schlumberger and dipole–dipole electrode configurations, as discussed in more detail below. The observed pseudosection is shown in the top panel of Figure 4.17. The larger solid squares at the top of the pseudosection correspond to electrode locations while the smaller symbols that appear in the interior of the pseudosection mark the locations where the measured apparent resistivity is plotted. The pseudosection is displayed by contouring the apparent resistivity data. The trapezoidal shape of the pseudosection reflects the fact that the measured data are only minimally sensitive to ground structure in the two triangular regions beneath either the current or the potential electrodes.

4.7 Electrical-resistivity tomography (ERT)

Traditional electrical-resistivity soundings use a conventional electrode configuration such as Schlumberger, Wenner, dipole–dipole, pole–dipole, or pole–pole (see Figure 4.8). A sounding, in which the electrode-separation lengths are varied without moving the array

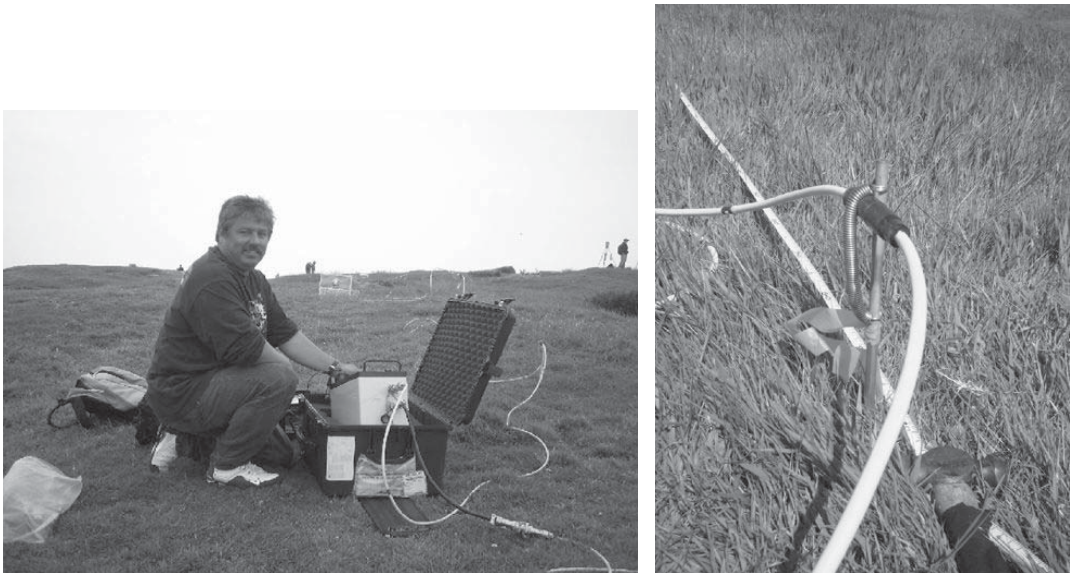

Figure 4.16 (Left) Multi-electrode resistivity system from AGI Geosciences, Inc.; (right) close-up of an electrode installation.

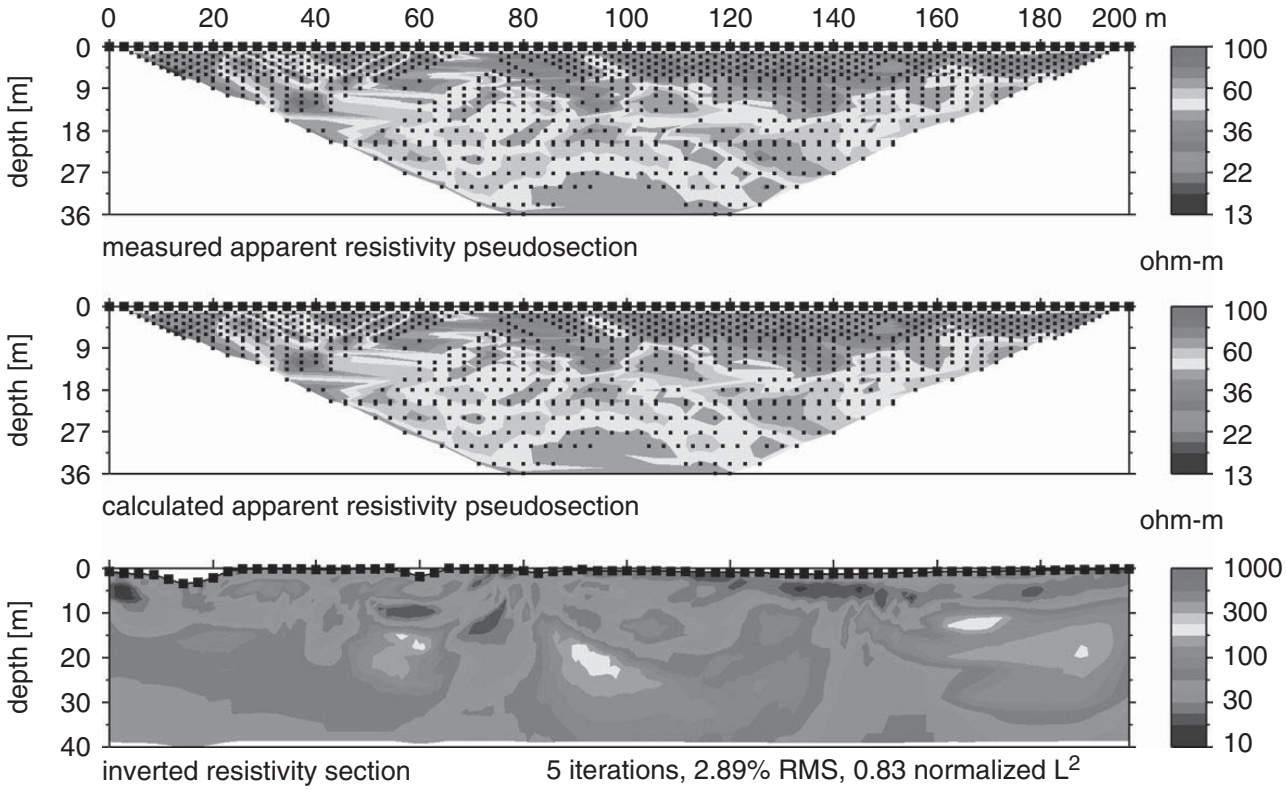

Figure 4.17 Measured apparent resistivity pseudosection (top) for a hybrid Schlumberger-DD electrode configuration, along with the inverted resistivity image (bottom). The calculated pseudosection (middle) is based on solving the forward problem for the resistivity structure shown at the bottom. Note the good match between the measured and calculated pseudosections.

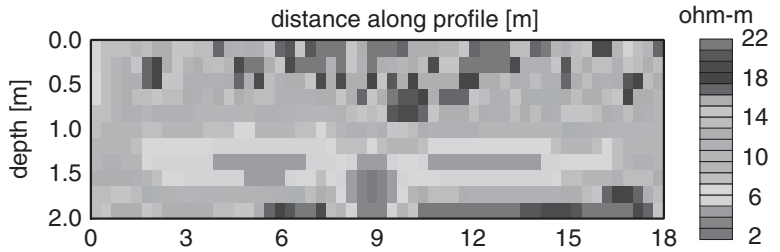

Figure 4.18 Inversion of dipole-dipole resistivity data acquired over a buried pipeline at the Texas A&M Riverside campus. The pipeline is the conductive (*red*) zone at depth 1.5–2.0 m midway along the profile. Electrode spacing is 0.3 m.

midpoint, provides a local 1-D electrical-resistivity depth model, $\rho(z)$. Alternatively, lateral profiling of $\rho(x)$ over a narrow depth interval can be achieved by traversing the electrode array along a horizontal profile without changing the electrode separations. Neither the sounding nor the profiling method alone provides an accurate indication of subsurface resistivity distribution in complex geological terrains.

Resistivity imaging of complex subsurface structures has recently advanced with the development of multi-electrode acquisition systems and 2-D and 3-D inversions. The resistivity technique for near-surface applications has surged in popularity due to these advances. Pioneering work on electrical-resistivity tomography (ERT) was published by Daily and Owen (1991) who considered a cross-borehole electrode configuration.

ERT imaging is performed by matching the measured apparent resistivity pseudosection to a computed pseudosection that is obtained by solving, for a given Earth resistivity structure $\rho(\mathbf{r})$, the governing scaled-Laplace equation $\nabla\cdot([1/\rho]\nabla\varphi) = 0$. The electric-potential distribution $\varphi(\mathbf{r})$ is evaluated at the locations of the potential electrodes and then transformed into a computed apparent resistivity. The model $\rho(\mathbf{r})$ is then adjusted, and the apparent resistivity re-computed, ideally until it matches the measured apparent resistivity to within a pre-defined acceptable tolerance. The process of forward modeling and imaging is discussed in detail in later chapters of this book. The bottom two panels of Figure 4.17 show a resistivity image and its calculated apparent resistivity response. The spatial structure of the resistivity image, in this example, reflects variations in subsurface moisture content.

A second field example of ERT imaging is shown in Figure 4.18. A dipole–dipole data set was acquired along a profile over a buried pipeline on Riverside campus at Texas A&M University. The inversion algorithm dc2dinv, which is available at www.resistivity.net, was used to construct the image. The profile uses 56 electrodes and is oriented orthogonal to the strike of the target with 0.3-m electrode spacing. The signature of the pipeline is the low-resistivity zone that appears at the midpoint of the profile, at depth ~ 2 m beneath the surface. The laterally variable structure that is evident in the upper part of the image (depths < 0.5 m) is likely caused by near-surface soil heterogeneity and irregular coupling of the electrodes to the ground.

There is a possibility for interpretation errors to occur if ERT data are aquired on a sparse set of orthogonal 2-D lines or transects and then subjected to fully 3-D modeling and inversion. Gharibi and Bentley (2005) recommend that to avoid artifacts the line spacing

should be not more than two–four times the electrode spacing. Measurements should be made, if possible, using a wide range of azimuths of the line joining the midpoints of the current–electrode pair and the potemtial–electrode pair. Furthermore, the electrode spacing should not be greater than the dimensions of the smallest feature to be imaged.

4.8 Electrical properties of rocks

In the shallow subsurface, the most important geological factor that controls the bulk electrical resistivity is the spatial distribution of pore-fluid electrolytes. The aqueous pore fluids may be contained in pores, fractures, or faults. Electrical geophysical investigations have been used in various hydrogeological, environmental, geotechnical, and civil-engineering applications.

A fundamental assumption of the electrical and electromagnetic methods of geophysics, including the electrical-resistivity technique, electromagnetics (EM), and ground-penetrating radar (GPR), is that the underlying geological medium is electrically neutral, containing vast but equal numbers of positive and negative charge carriers. Some of the charges are free or quasi-free to migrate, or drift, from place to place within the geological medium. Other charges are bound to lattice atoms or other microscopic, localized "charge centers" (Jonscher, 1977), or they are held at material interfaces. Bound charges play no role in the electrical-resistivity or EM techniques but as the reader will see in later chapters they are significant in shaping GPR, induced polarisation (IP), and self-potential signals. Electrical conductivity σ measures the capability of a material to sustain long-term current flow via the charge migration mechanism. By longstanding convention, the electrical resistivity $\rho = 1/\sigma$ is the material parameter used to interpret data acquired using the electrical-resistivity technique but herein we use conductivity and resistivity interchageably. Two significant types of charge polarization, atomic and molecular, and two types of charge migration, semi-conduction and electrolytic conduction, are illustrated in Figure 4.19.

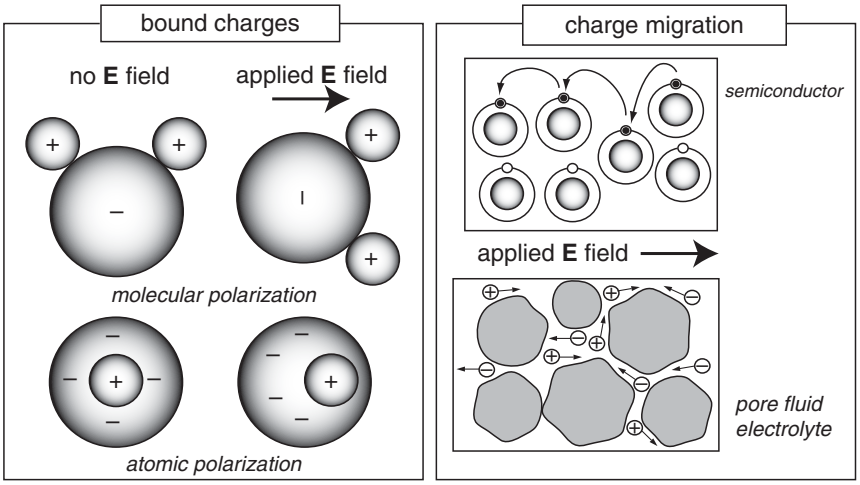

Figure 4.19 Electrical-polarization (left) and -migration (right) mechanisms.

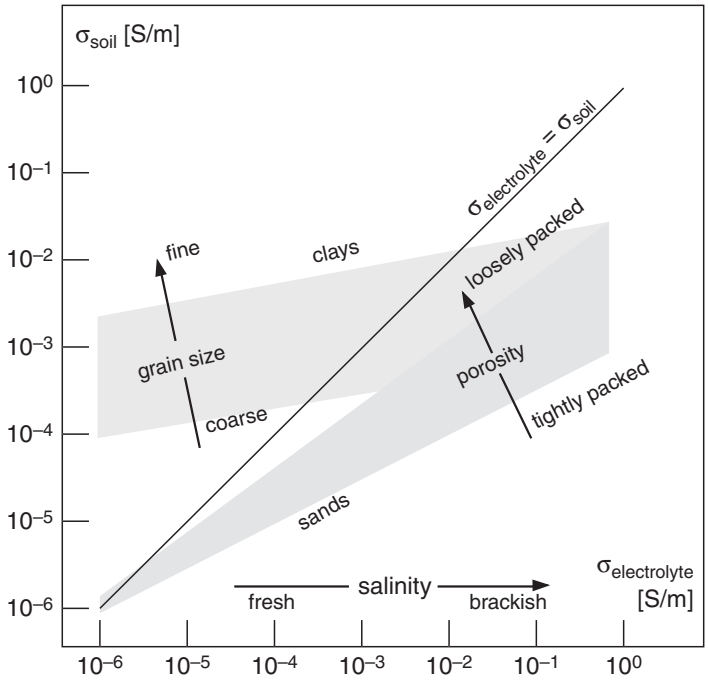

Figure 4.20 Electrical conductivity of saturated soils, after Santamarina *et al*. (2005).

Electrical conduction in most rocks is *electrolytic*, with ions in the pore fluids being the predominant charge carriers. The solid matrix of grains is typically semi-conducting, with notable exceptions being metallic grains and the surface of certain clay minerals, which are conducting. The pore space in a rock is generally much more conductive than the solid grains owing to the presence of dissolved ions in the pore-fluid solution.

Electrolytic conductivity increases, or equivalently, resistivity decreases with increasing salinity, porosity ϕ, and temperature T. A high-salinity pore fluid has a greater concentration of ions available for conduction; a rock with high interconnected porosity often has an abundance of paths for conduction; higher temperature enhances the mobility of ions. The variation of bulk electrical conductivity as a function of salinity, for sand-dominated and clay-dominated saturated soils, is outlined in Figure 4.20.

Purely siliciclastic rock units such as clean, unfractured sandstones typically exhibit a fairly regular intergranular, or primary, porosity that developed as the original sediment compacted and lithified. The pore space in such rocks usually forms an interconnected network with open intergranular spaces that are connected by clear throats. A well-sorted sandstone of this type has a high permeability.

In clean, unfractured sandstones characterized by water saturation S_W and porosity ϕ, the traditional Archie's law (Archie, 1942) gives the bulk electrical conductivity σ [siemens per meter, S/m] as

$$\sigma = a\sigma_W S_W^n \phi^m. \tag{4.37}$$

This empirically based relationship with saturation exponent $n \sim 2$ has long been used by petroleum geoscientists and more recently by hydrogeophysicists to describe the bulk

electrical conductivity σ of hydrocarbon reservoirs and aquifers. The parameter m, historically known as the cementation exponent, depends on the grain shape and generally lies within the range $m \sim 1.2$–2.2 for sandstones (Worthington, 1993). The leading coefficient a can vary widely depending on the pore cementation, tortuosity, grain size and shape, fluid wettability, clay content, and numerous other factors.

The quantity $\sigma_W \sim 0.3$–1.0 S/m (Keller and Frischknecht, 1966) in Equation (4.37) is the electrical conductivity of the pore electrolyte, which is controlled by the salinity, or more generally the total dissolved solids in the pore water. Commonly, an intrinsic formation factor $F = \sigma_W/\sigma$ for a fully water-saturated ($S_W = 1$) rock unit is defined. Since pore fluids are electrically conductive relative to the solid rock matrix, we have $\sigma_W > \sigma$ and hence $F > 1$. From Archie's law (4.37), for a fully saturated rock we see that the formation factor is related to porosity by $F \sim \phi^{-m}$.

Clay minerals originating from secondary diagenetic processes can coat the sand grains and clog the pore throats, reducing the porosity and permeability. A general rule of thumb is that high-porosity sandstones are likely to be clean while low-porosity sandstones are likely to be shaly. Clay minerals also have an inherent negative surface charge which contributes an additional electrical conduction pathway that is not found in clean sandstones. Thus, clay-bearing formations generally have a considerably higher bulk electrical conductivity than clean sandstones.

Waxman and Smits (1968), Worthington (1993), and others have demonstrated that important modifications to Archie's formula are necessary in the case of shaliness. These studies suggest that the intrinsic formation factor $F = \sigma_W/\sigma$ should be regarded only as an *apparent* formation factor F_a and that shale effects might be responsible for much of the observed variability in the Archie parameters (a, m). The shale effect on the formation factor is described by the Waxman–Smits equation

$$F_a = F\left[1 + \frac{\tilde{\sigma}}{\sigma}\right]^{-1} = \frac{\sigma_W}{\sigma + \tilde{\sigma}}, \tag{4.38}$$

where $\tilde{\sigma}$ is the "excess conductivity" of the rock that accounts for the surface conduction associated with the clay particles, including the effects of the cation-exchange reactions that occur between the clay and the saturating electrolye. Numerical values for $\tilde{\sigma}$ can be computed from basic electrochemical tables if the composition and concentration of the saturating electrolyte is known. When shale effects are absent, $\tilde{\sigma} \to 0$ and $F_a \to F$ in Equation (4.38), as expected.

Geological interpretation of resistivity data is more problematic in carbonate terrains than in sands. Carbonate rock units commonly exhibit secondary porosity, such as moldic vugs caused by anhydrite dissolution of fossil remains, that develop after the rock is formed. The secondary porosity can carry a considerable fraction of the permeability. The bulk permeability depends strongly on whether the vugs are separate or touching each other (Lucia, 1983). It is very difficult to make an assessment from studying outcrops and drilled core samples about the role of vugs in shaping the bulk hydrogeological behavior of a carbonate formation. Furthermore, the range of intergranular textures found in carbonate rocks varies greatly from coarser grain-dominated to finer mud-dominated fabrics.

In carbonates, the relationship between electrical resistivity and porosity is quite complicated (Summers, 2006). Archie's law has limited predictive value in carbonates as the m value can vary widely and it is difficult to ascertain for a given formation. Cementation exponent values as high as $m \sim 4$–7 have been observed in Middle East oil reservoirs. Asquith (1995) has noted that large values of m are associated with higher separate-vug porosities, while a lower m value is associated with touching-vug porosity, such as fractures.

4.9 Electrical–hydraulic field-scale correlation studies

A long-standing debate amongst near-surface geophysicists has arisen about whether it might be possible to interpret geoelectrical measurements in terms of aquifer bulk properties. Resolution of this issue is one of the main focus points of the rapidly expanding field of hydrogeophysics (Slater, 2007). The capability to convert electrical geophysical data into estimates of bulk aquifer properties such as transmissivity or storativity, for example, would represent a major breakthrough in the field of water-resources research.

Many laboratory studies over the past several decades have claimed to discover links between electrical and hydraulic properties of rock samples. Early investigations by Katz and Thompson (1986), for example, received a great deal of attention. They proposed a relationship of the form

$$k \sim \frac{l_c^2}{226}\left(\frac{\sigma}{\sigma_W}\right), \tag{4.39}$$

where k [darcies, D = μm^2] is the fluid permeability, l_c [μm] is a characteristic length of the pore space, and σ is the electrical conductivity of a rock sample saturated with a brine solution of electrical conductivity σ_W. Katz and Thompson (1986) explain how l_c is determined in the laboratory from mercury-injection experiments.

Equation (4.39) suggests that a positive correlation exists between the fluid-transport property k and electrical conductivity. Huntley (1986) has shown however that the electrical–hydraulic (σ, k) relation in rock samples can also be negatively correlated. The latter case is readily understood in clay-bearing samples where the presence of clay increases the bulk electrical conductivity, due to enhanced surface conduction effects, but at the same time decreases the bulk fluid permeability since clay particles generally clog the pores. A good discussion of the complexities involved in establishing petrophysical relationships between electrical and hydraulic properties, at the sample scale, is provided by Lesmes and Friedman (2005).

While laboratory experiments can provide a fundamental basis for understanding electric–hydraulic correlations at the sample length scale (~ 0.1–10 cm), of greater interest here are linkages at much larger field scales (~ 10 m–1 km) between geoelectrical measurements and aquifer properties.

A simple interpretive rule, which strictly applies only under ideal geological conditions, has been suggested by MacDonald *et al*. (1999). Consider a clean, sandy aquifer. Standard hydrological theory predicts, in this case, a direct relation between porosity ϕ and hydraulic conductivity K. Furthermore, based on Archie's law (4.37), an inverse relation is expected between porosity ϕ and resistivity σ, where σ is the reciprocal of conductivity σ. Thus, in idealized clay-free aquifers the product $K\sigma$ is approximately constant. On the other hand, it is well known that in clay-rich aquifers the hydraulic conductivity and electrical resistivity are both controlled by the clay content rather than the porosity. Since K and σ both increase in direct relation to the clay content, to first order, we have that the quotient K/σ should remain roughly constant in ideal clay-rich aquifers.

MacDonald *et al*. (1999) rely on the foregoing analysis to relate a bulk aquifer property to the bulk electrical resistivity inferred from surface-based electrical geophysical measurements. Consider the aquifer transmissivity $T = Kh$, where h is the aquifer thickness. Suppose also that a 1-D-layered resistivity sounding curve has been acquired over the aquifer. Such a curve could be constructed, for example, from an inversion of Schlumberger or dipole–dipole apparent-resistivity measurements. If the resistivity of the layer that corresponds to the aquifer is comparatively high, the aquifer is likely to have a low clay content and it can be shown that the best-resolved geoelectrical parameter is the transverse resistance $R_t = h\sigma$ of the layer. Similarly, the longitudinal conductance $L_c = h/\sigma$ is the best-resolved parameter in the case of a clay-rich, comparatively conductive layer.

For the clay-free aquifer, we can combine the finding that $K\sigma$ is constant with the definitions $R_t = h\sigma$ and $T = Kh$ to deduce that

$$T = C_1 R_t. \tag{4.40}$$

In other words, the aquifer transmissivity is in direct proportion to the geophysically determined transverse resistance of the aquifer. Similarly, for the clay-rich aquifer it follows that

$$T = C_2 L_C, \tag{4.41}$$

or the transmissivity is in direct proportion to the longitudinal conductance. The appropriate constant C_1 or C_2 can be determined by comparing the resistivity sounding curve to hydraulic data at locations where the transmissivity has been determined by pump tests. Then, using geophysics and either Equation (4.40) or (4.41) depending on the aquifer type, an estimate of the aquifer transmissivity can be extrapolated to areas outside the region of influence of the available pump tests. This is a valuable exercise since pump tests are much more expensive to carry out than surface geophysical measurements. MacDonald *et al*. (1999) have used this method to estimate the spatial distribution of transmissivity of the gravel aquifer at Desborough Island on the Thames River near London. The result is shown in Figure 4.21.

A different approach for interpreting geoelectrical measurements in terms of aquifer properties was suggested by Soupios *et al*. (2007) who combined information from wells with 1-D inversions of Schlumberger vertical electric sounding data acquired at a number

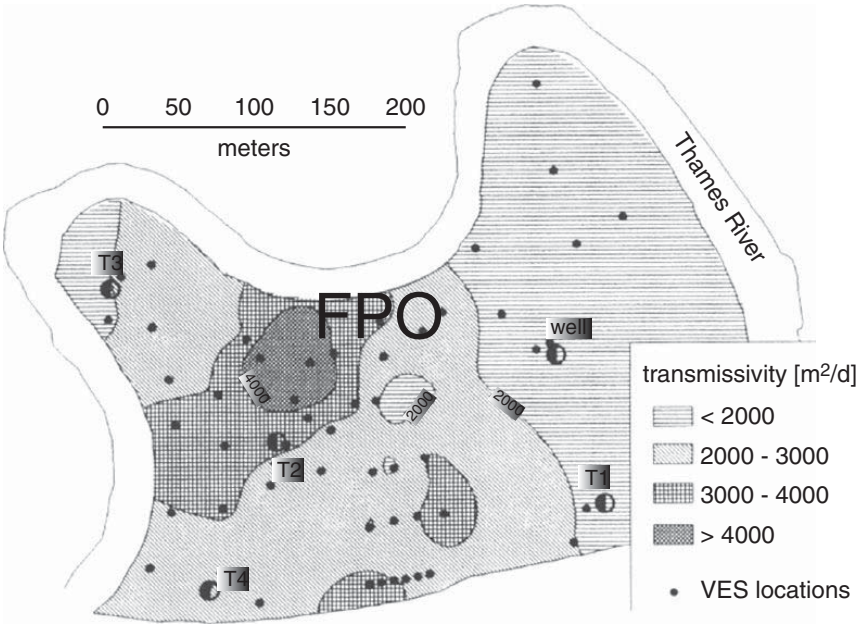

Figure 4.21 Transmissivity of the subsurface gravel aquifer at Desborough Island, UK. Point estimates are obtained from pump tests at locations T1–T4. Spatially distributed estimates are obtained from ~ 50 electrical geophysical soundings (VES), marked by the small black dots. After MacDonald *et al*. (1999).

of sites on the island of Crete. The conversion from resistivity to hydraulic conductivity was performed using the geophysically inferred value of the porosity ϕ, as follows. In the clay-bearing aquifer at Crete, Archie's law (4.37) no longer applies and consequently the Waxman–Smits equation was used. Re-arranging Equation (4.38) gives

$$\frac{1}{F_a} = \frac{1}{F} + \tilde{\sigma}\,\rho_W, \tag{4.42}$$

such that a plot of the inverse of the apparent formation factor F_a against the pore-fluid resistivity σ_W yields an intercept of $1/F$. The apparent formation factor F_a at each sounding location on Crete was evaluated using bulk resistivity σ from inversion of the Schlumberger data along with the fluid resistivity σ_W measured from a nearby well. The intrinsic formation factor F was obtained from a linear regression based on Equation (4.42), and then converted into porosity ϕ using Archie's law. Then the hydraulic conductivity k [m/day] of the aquifer was computed using the standard hydrology equation (Domenico and Schwartz, 1990)

$$k = \frac{480\delta_W g d^2 \phi^3}{\mu(1-\phi)^2}, \tag{4.43}$$

where d [m] is the grain size, $g = 9.80$ m/s^2 is gravity, $\delta_W = 1000$ kg/m^3 is the fluid density, and $\mu = 0.0014$ kg/m s is the fluid dynamic viscosity. Finally, the aquifer transmissivity $T = kh$ [m^2/d] was evaluated using Equation (4.43) along with the known thickness of the aquifer obtained from the nearby wells. The resulting spatial distribution of aquifer transmissivity is shown in Figure 4.22.

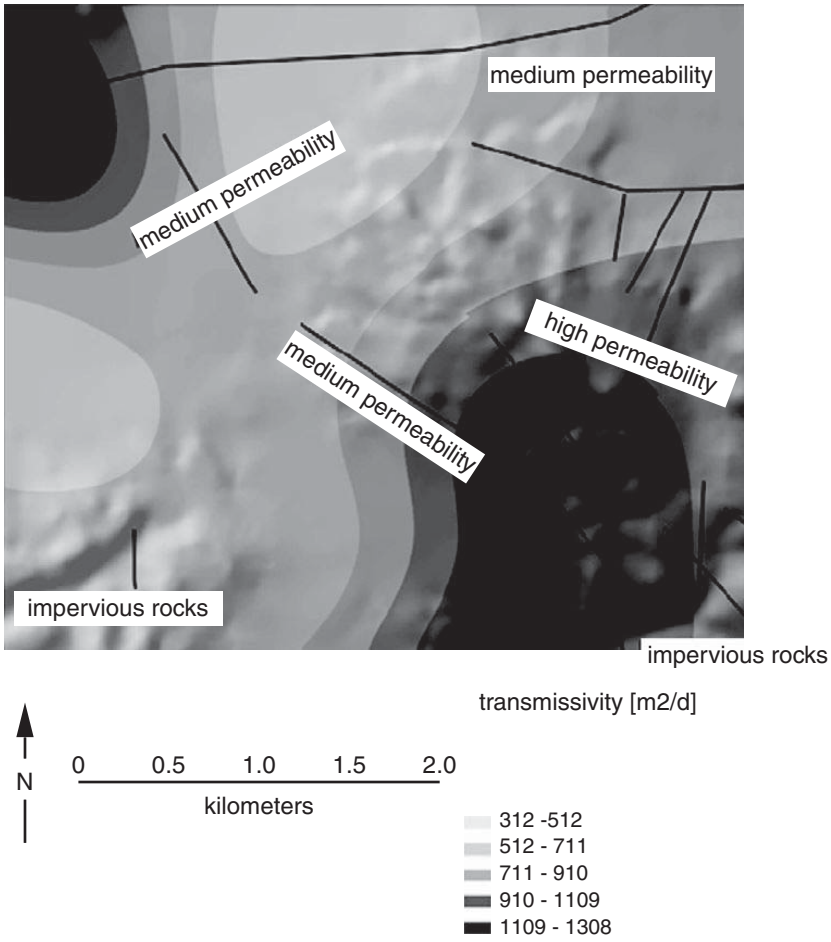

Figure 4.22 Transmissivity of the Keratis basin aquifer in Crete based on Schlumberger electrical soundings. After Soupios *et al*. (2007).

4.10 Optimal electrode placement

Extensive field tests and sensitivity studies have indicated that each of the traditional electrode configurations has strengths and weaknesses. With the advent of computer-controlled multi-electrode acquisition capabilities (e.g. Loke, 2000), data can be recorded using a variety of standard and non-standard configurations. The combined dataset can then be inverted to obtain a 2-D or 3-D subsurface model.

Consider a linear array of d equally spaced electrodes. There are a total of

$$D = d(d-1)(d-2)(d-3)/8 \tag{4.44}$$

possible four-point (one current source, one current sink, and two potential measurement) electrode configurations. For example, if $d = 50$ electrodes are laid out, this leads to $D =$ 690 000 possible four-point measurements, each of which takes $\sim$ 1 s to acquire.

Commercial systems routinely use $d > 100$ electrodes. Thus, acquisition of a *comprehensive dataset* of D responses is impractical.

It is of interest, therefore, to determine whether limited combinations of electrode configurations can supply subsurface resistivity images that are comparable in quality to images that would be generated from a comprehensive dataset. An experimental design procedure has been developed by Stummer *et al*. (2004) to achieve this goal. A non-linear objective function is defined and maximized using a global optimization technique.

The performance of traditional electrode configurations is evaluated using a synthetic model (Figure 4.23a, left panel) consisting of a thin, moderately conductive ($\rho = 100$ Ωm, typical of silt) near-surface layer overlying a resistive ($\rho = 1000$ Ωm, typical of dry gravel) basement. A highly conductive ($\rho = 10$ Ωm) block and a highly resistive ($\rho = 10\,000$ Ωm) block are embedded in the model to provide lateral heterogeneity, as shown.

A simulated resistivity configuration using $d = 30$ (such that $D = 82\,215$) electrodes with spacing $\Delta x = 5$ m is deployed along the top of the model. Omitting certain combinations that yield intrinsic poor data quality, such as crossed-dipole and very-long-offset dipole–dipole configurations, a simulated data set of size $D = 51\,373$ is generated using a standard finite-difference modeling code. The synthetic data $\mathbf{d}_{OBS}$, consisting of logarithmic voltage readings, are then inverted (see Chapters 11–13) using an iterative scheme

$$\mathbf{m}_{i+1} = \mathbf{m}_i + G^{-g}(\mathbf{d}_{OBS} - \mathbf{d}[\mathbf{m}_i]) \tag{4.45}$$

where $\mathbf{m}_i$ is a vector of parameters which describe the resistivity model, and $\mathbf{d}[\mathbf{m}_i]$ is the computed data based on model $\mathbf{m}_i$.

The quantity $G^{-g} = (G^T G + C_M^{-1})^{-1} G^T$ is the generalized stable inverse of the Jacobian matrix $\mathbf{G}$ defined by

$$G_{ij} = \frac{\partial ln V_i}{\partial ln \rho_j}, \tag{4.46}$$

and $\mathbf{C}_M$ is the model covariance matrix, which includes damping or smoothing constraints on the model parameters. In Equation (4.46), ρ_j is the electrical resistivity of the j-th model cell of the total of P cells. Thus, the dimension of matrix G is $D \times P$. Inversion results for the synthetic test model are shown in Figure 4.23b–e, left panel. Note that the best model recovery is associated with the comprehensive data set. The conductive body at the left is not seen using the Wenner and/or dipole–dipole data sets.

In the experimental design procedure of Stummer *et al*. (2004), a homogeneous half-space of uniform resistivity is used as a starting model. Assume an initial data set of size $D_0 << D$, based on a traditional array such as dipole–dipole. The key design step is to determine which additional electrode configurations would provide the most new information about the subsurface. A quantitative measure of information is provided by the Jacobian sensitivity matrix.

Suppose that the 2-D resistivity model consists of $P = pq$ cells. The Jacobian of the comprehensive dataset is denoted by G^C. The Jacobian of the initial data set is G^0. The two Jacobians have dimensions $dim G^C = D \times pq$ and $dim G^0 = D_0 \times pq$, respectively. We can define a new $(D - D_0) \times pq$ matrix G^1 according to $G^C = [G^0 | G^1]$, which corresponds to

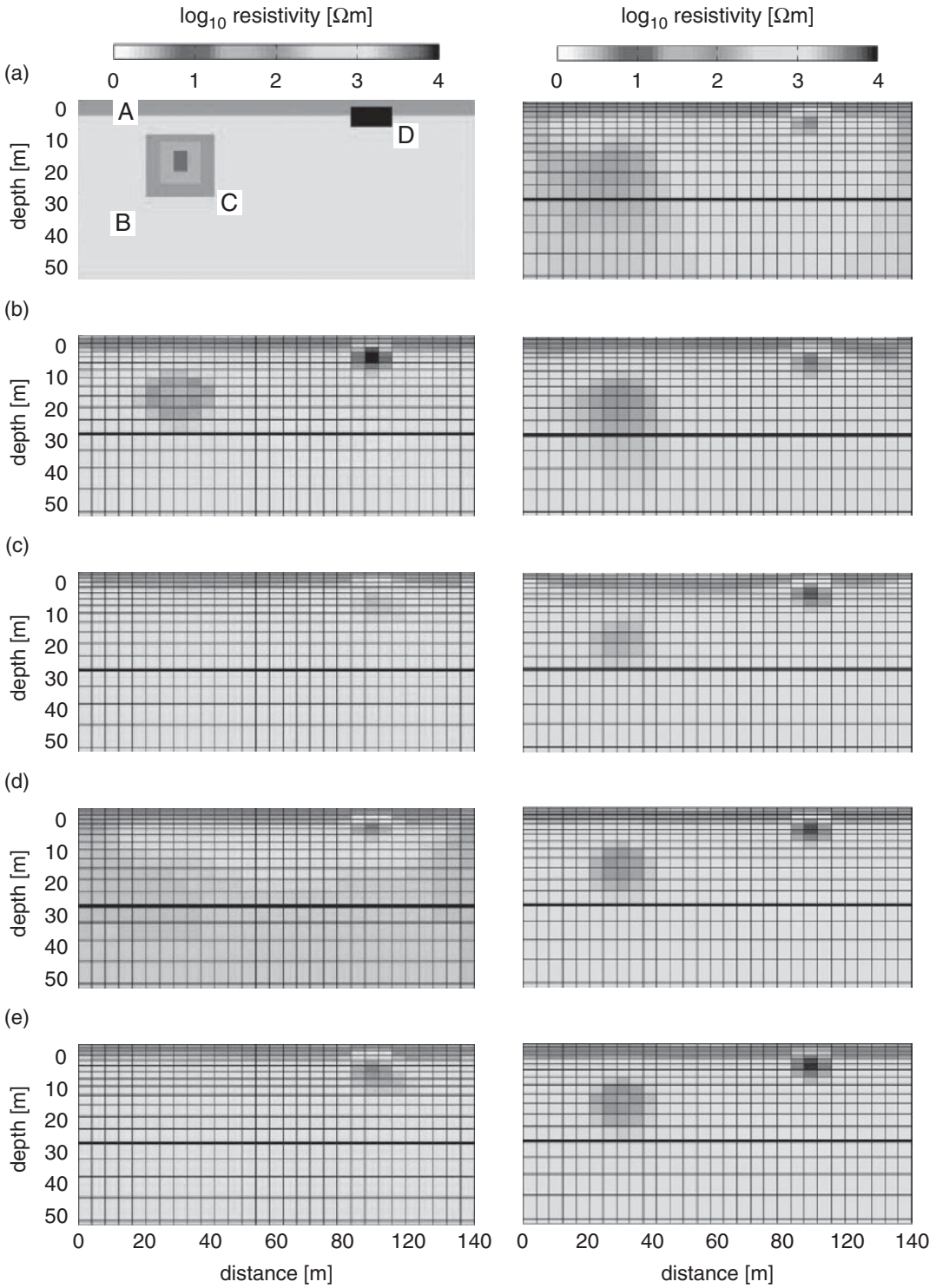

Figure 4.23 (Left panel) Resistivity inversion test, after Stummer *et al*. (2004), (a) starting model. Inversion results using: (b) comprehensive dataset, $D = 51\,373$; (c) Wenner $D = 135$; (d) dipole–dipole $D = 147$; (e) Wenner/dipole–dipole $D = 282$ electrode configurations. (Right panel) Resistivity inversion based on optimal experimental design, after Stummer *et al*. (2004), (a) $D = 282$; (b) $D = 670$; (c) $D = 1050$; (d) $D = 5740$; (e) $D = 10\,310$ electrode configurations.

the remaining, unacquired dataset. We can also define the resolution matrices $R^C = (G^C)^{-g} G^C$ and $R^0 = (G^0)^{-g} G^0$. The i-th electrode configuration in the unacquired dataset is considered to provide important information if it generates a large value of the *goodness function* $\Psi(i)$, where

$$\Psi(i) = \sum_{j=1}^{pq} \frac{|G_{ij}^1|}{G_j} \left[1 - \frac{R_{jj}^0}{R_{jj}^C} \right]. \tag{4.47}$$

The normalization factor

$$G_j = \frac{1}{D} \sum_{i=1}^{d} |G_{ij}^C| \tag{4.48}$$

compensates for the natural tendency of near-surface cells to dominate the sensitivity calculation. Note that $\Psi(i)$ is large when the elements of the corresponding row of matrix G^1 are large. Since a diagonal element $R_{jj} = 1$ indicates a perfect resolution of the j-th model parameter, the term $1 - R_{jj}^0 / R_{jj}^C$ appearing in Equation (4.47) forces the goodness function $\Psi(i)$ to favor electrode configurations that can constrain unresolved model parameters.

The goodness function $\Psi(i)$ in Equation (4.47) is only one of many that could be usefully defined in an optimal experimental design. We can rank the electrode configurations in the unacquired dataset according to their values of the goodness function. The ones that generate the highest goodness function are then used to generate the next dataset. An electrode configuration is rejected if it is linearly independent (as determined by their respective rows in the comprehensive Jacobian matrix) to a configuration used in the initial dataset. An example of optimized inversion using the synthetic example is shown in Figure 4.23, right panel.

4.11 Underwater resistivity techniques

A review of developments in marine electrical and electromagnetic geophysical techniques, including resistivity, IP, and EM methods, is provided by Butler (2009). A summary of the literature shows that there has developed in recent years two common modes of operation for underwater resistivity surveys. In a mode of operation (Day–Lewis *et al.*, 2006; Passaro, 2010) that is particularly suited for a number of shallow-water applications including mapping coastal freshwater discharge and nautical archaeology, an array of floating electrodes is towed on the water surface behind a vessel (Figure 4.24). Such systems can achieve continuous resistivity profiling of the subbottom resistivity structure and have detected seabed anomalies caused by shipwrecks. Other studies have attempted to use bottom-towed electrode arrays but these can be easily damaged as they are dragged across the rugged seafloor.

In another mode of operation, the electrode array is stationary. In some cases an array of grounded electrodes is employed that makes direct electrical contact with the subbottom, as in conventional land surveys. In deeper water, electrodes may be suspended on vertical cables extending from buoys or a vessel at the sea surface into the water column. This approach was used by Baumgartner and Christensen (1998). The choice of which marine